Acoustomicrofluidic Defect Engineering and Ligand Exchange in ZIF-8 Metal–Organic Frameworks

Emily Massahud, Heba Ahmed, Ravichandar Babarao, Yemima Ehrnst, Hossein Alijani, Connie Darmanin, Billy J. Murdoch, Amgad R. Rezk, and Leslie Y. Yeo*

A way through which the properties of metal–organic frameworks (MOFs) can be tuned is by engineering defects into the crystal structure. Given its intrinsic stability and rigidity, however, it is difficult to introduce defects into zeolitic imidazolate frameworks (ZIFs)—and ZIF-8, in particular—without compromising crystal integrity. In this work, it is shown that the acoustic radiation pressure as well as the hydrodynamic stresses arising from the oscillatory flow generated by coupling high frequency (MHz-order) hybrid surface and bulk acoustic waves into a suspension of ZIF-8 crystals in a liquid pressure transmitting medium is capable of driving permanent structural changes in their crystal lattice structure. Over time, the enhancement in the diffusive transport of guest molecules into the material's pores as a consequence is shown to lead to expansion of the pore framework, and subsequently, the creation of dangling-linker and missing-linker defects, therefore offering the possibility of tuning the type and extent of defects engineered into the MOF through the acoustic exposure time. Additionally, the practical utility of the technology is demonstrated for one-pot, simultaneous solvent-assisted ligand exchange under ambient conditions, for sub-micron-dimension ZIF-8 crystals and relatively large ligands—more specifically 2-aminobenzimidazole—without compromising the framework porosity or overall crystal structure.

1. Introduction

Zeolitic imidazolate frameworks (ZIFs), which comprise tetrahedrally-coordinated single-metal ions linked to imidazole derivates,[1,2] are a subclass of metal–organic frameworks (MOFs) that exploit the inherent advantages of zeolites (e.g., their thermal and chemical stability, and abundance of acid sites that bestow them with high catalytic activity), while also being endowed with the advantages of MOFs in general, such as their high porosity and surface area, and tunable linker diversity. As such, ZIFs, of which ZIF-8 [$Zn(mIm)_2$, where mIm = 2-methylimidazolate] is arguably the most-well studied given its intrinsic stability, have demonstrated significant potential for applications across catalysis,[3] gas separation,[4] and chemical sensing.[5]

The judicious introduction of structural defects in MOFs in a controlled and targeted manner offers a way by which the surface and electronic

E. Massahud, H. Ahmed, Y. Ehrnst, H. Alijani, A. R. Rezk, L. Y. Yeo
Micro/Nanophysics Research Laboratory
RMIT University
Melbourne, VIC 3000, Australia
E-mail: leslie.yeo@rmit.edu.au

R. Babarao
Manufacturing Business Unit
Commonwealth Scientific and Industrial Research Organization (CSIRO)
Manufacturing
Clayton, VIC 3168, Australia

R. Babarao
Centre for Advanced Materials and Industrial Chemistry, School of Science
RMIT University
Melbourne, VIC 3000, Australia

C. Darmanin
Department of Mathematical and Physical Sciences
School of Engineering
Computing and Mathematical Sciences
La Trobe University
Melbourne, VIC 3086, Australia

C. Darmanin
La Trobe Institute for Molecular Science
La Trobe University
Melbourne, VIC 3086, Australia

B. J. Murdoch
RMIT Microscopy and Microanalysis Facility
STEM College
RMIT University
Melbourne, VIC 3000, Australia
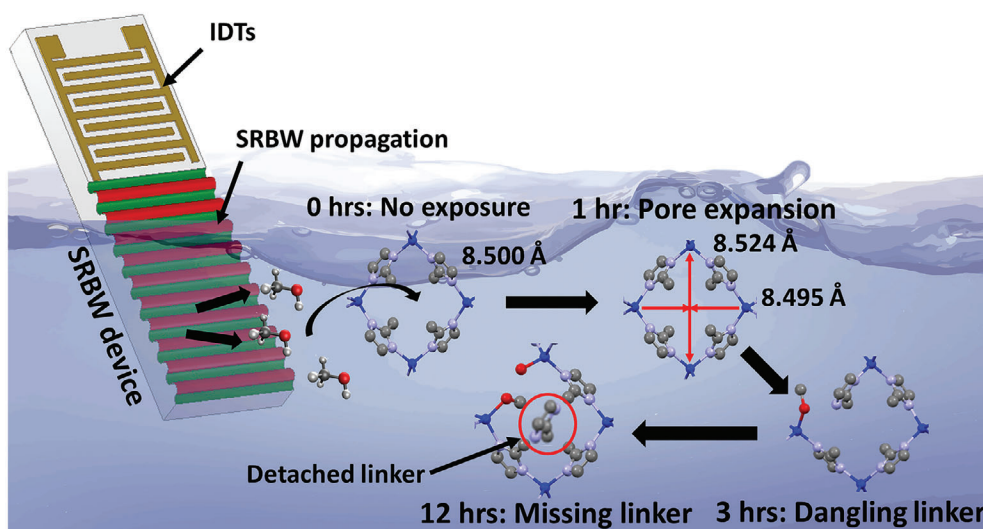
Figure 1. Schematic illustration of the experimental setup for acoustomicrofluidic defect creation. The device, which is partially immersed in a suspension of pre-synthesized ZIF-8 crystals (here depicted as a cross-section of the crystal lattice at the pore aperture) in a pressure transmitting medium (methanol), comprises a piezoelectric (lithium niobate; $LiNbO_3$) chip, on which the SRBW is generated by applying an AC electric field at resonance (10 MHz) to the interdigitated transducers (IDTs) patterned on the substrate. The transmission of the SRBW energy into the medium generates an oscillatory flow that imparts hydrodynamic stresses on the crystals, which together with the acoustic radiation pressure, enhances diffusion of guest molecules into its pores. This, in turn, results in the expansion of its pores at 1 h of exposure, as shown by the red arrows, and subsequently, the creation of dangling-linker (and methanol inclusion) and missing-linker defects at 3 and 12 h, respectively.

properties or intrinsic porosity of the MOF can be tuned in order to improve its performance for various applications.[6–9] As an example, one way by which such defects can be introduced is through the breaking and reorganizing of the bonds in the structure, or distorting its lattice, to remove a portion of, or the entire, linker to respectively create "dangling" or "missing" linkers. A variety of defect engineering strategies have been developed to date,[10] which can be broadly categorized into chemical, thermal and mechanical methods. While the use of chemical methods[11,12] and modulators in defect engineering has been widely reported and generally affords control over the number of defects, stringent care is required to avoid compromising overall crystal quality due to pore collapse and amorphization.[13,14] Thermal annealing, on the other hand, intrinsically suffers from low reproducibility[8,15,16] due to difficulties in systematically controlling defect creation, and can often lead to cross contamination from combustion by-products or partial carbonization of the material.[16] Similarly, the imposition of intense mechanical stresses—for example, by ball milling the sample—is an effective chemical-free method for introducing defects, although often at the expense of pore collapse or amorphization.[17]

The most common mechanical means of introducing defects into MOFs is through the use of an anvil cell, in which hydrostatic compression is applied to the sample through a pressure transmitting medium. For ZIF-8, pressures of ≈1.5 GPa and up to ≈4 GPa have been shown to induce rotation of the mIm linker that results in an enlargement of the cavity windows to facilitate accommodation of larger guest molecules.[18] Such "gate–opening,"[19–21] being a displacive phase transition,[22] however, falls short of constituting a defective structure, and the ZIF-8 structure typically relaxes upon removal of the compressive

stress. It is possible that higher pressures can lead to dangling-linker and missing-linker formation in ZIF-8 in aqueous solvents due to invasion of solvent molecules into its pores under pressure, resulting in the cleaving of the Z–N and C–N bonds.[23] However, the propensity of ZIF-8 to amorphization due to its low shear modulus, that consequently results in a reduction in its porosity, is also well-known at such high GPa-order pressures, unless guest molecules are present in its pores.[17,24–27] As such, the deliberate and controlled introduction of point defects into mechanically-rigid MOFs such as ZIF-8[28] at sufficiently high pressures to produce permanent defects, but without compromising their overall crystallinity, remains a significant challenge.[29,30]

Herein, we report a novel microfluidic defect engineering strategy in ZIF-8 that exploits the hydrodynamic pressure associated with the acoustically-driven oscillatory flow (acoustic streaming) arising from the coupling of high frequency (10 MHz order) nanometer amplitude hybrid sound waves in the form of surface reflected bulk waves (SRBWs)[31] into a solution of pre-synthesized ZIF-8 crystals suspended in methanol acting as a pressure transmitting medium (**Figure 1**); while SRBWs have previously been shown as a versatile technique for rapid and effective crystallization of novel morphologies and even MOFs,[32–35] they have not been reported to date as a means for defect engineering. Unlike the large GPa-order hydrostatic compression employed in the aforementioned mechanical defect engineering studies, the considerably gentler hydrodynamic stresses and MPa-order acoustic radiation pressure arising from the SRBW excitation allow for creation of defective ZIF-8 crystals at levels far below the critical stresses at which the material is typically known to amorphize. More specifically, we observe the
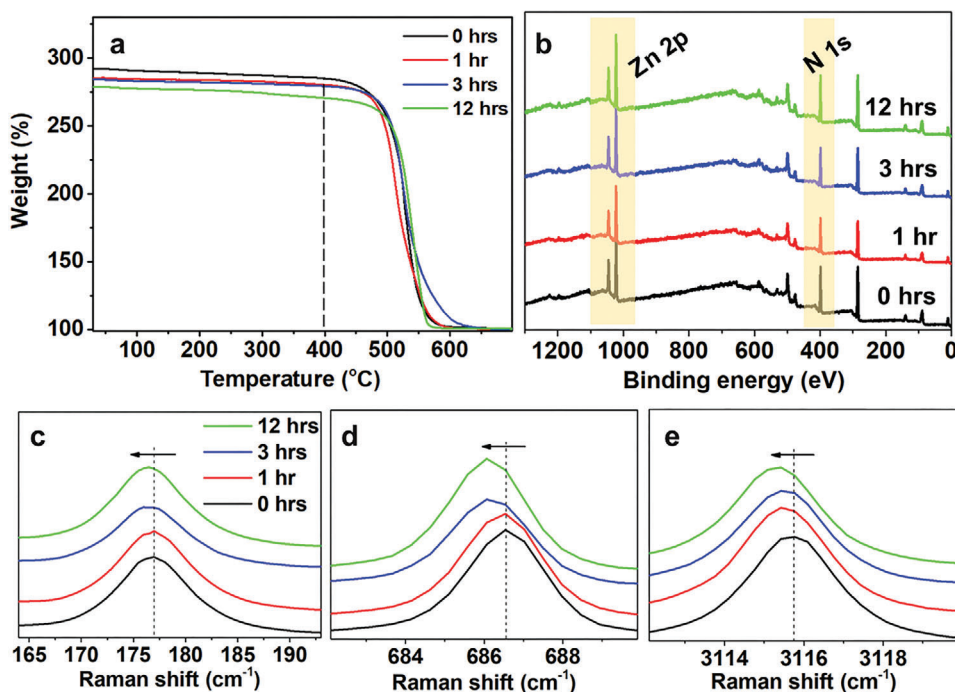
Figure 2. a) Thermogravimetric analysis (TGA), b) X-ray photoelectron spectra (XPS), and c–e) Raman spectra of ZIF-8 samples prior to (pristine control; 0 h) and following irradiation with the SRBW over different exposure durations. In (a), the final weights were normalized to 100%, corresponding to the remaining ZnO weight after pyrolysis; weight percentages at 400 °C were used to calculate the metal/linker ratios.[46] Panels (c–e) show red shifts, as indicated by the arrows, in the Raman vibrational modes, corresponding to Zn–N stretching, imidazole ring puckering and C–H (aromatic) stretching, respectively.

structures to progressively evolve through a number of different local defective states as they are continuously exposed to the SRBW forcing. Initial expansion of the framework due to pore stretching after 1 h of SRBW exposure, which produces a structure with increased pore accessibility, is then seen to give way to a framework that first contains dangling linkers after 3 h, followed by their detachment to form missing linker sites after 12 h—all at ambient temperature. Given such progressive evolution of the crystal through the various defective states, it is then possible to envisage tuning the system to achieve the desired "defect-by-design" by halting the process at the appropriate time.

We subsequently highlight the potential of this novel acoustic technique not only for post-synthetic defect engineering at ambient temperatures, but to also carry out, in the same step, solvent assisted ligand exchange (SALE)—a technique that allows the incorporation of different linkers into the framework, thereby constituting a versatile alternative for obtaining different MOF chemistries that cannot be produced through de novo syntheses.[36,37] Such an ability to simultaneously introduce defects into the crystal while concurrently substituting for the desired linker under ambient conditions limits any typical deterioration in gas uptake and porosity, and eliminates the need for harsh chemicals or lengthy processing.[38,39] Unlike other work to date on post-synthesis SALE of ZIF-8 with large linkers, which has typically been shown for small nanometer order (≈25 nm) crystals,[40,41] we demonstrate here the possibility for exchanging a large linker (2-aminobenzimidazole (2-AbIm)) into a relatively large sub-micron (≈0.3 μm) crystal, whilst retaining its crystallinity and surface area.

2. Results and Discussion

The experimental setup, in which the chipscale SRBW device is immersed within a methanol solution containing pristine, presynthesized ZIF-8 crystals to expose them to the nanometer amplitude hybrid surface and bulk waves in the form of the SRBWs, is schematically depicted in Figure 1; an image of the actual setup is shown in Figure S1, Supporting Information and details pertaining to the fabrication of the devices and the experimental procedure can be found in the Experimental Section. In particular, the SRBW generates a strong, continuous recirculatory flow, known as acoustic streaming,[42] that then subjects the ZIF-8 crystals to oscillatory hydrodynamic stresses and acoustic radiation pressures that are typically on the order of several MPa.

Characterization of the ZIF-8 crystals that were collected and dried following exposure to the SRBW over a prescribed duration (1, 3, or 12 h) through scanning electron microscopy (SEM) and powder X-ray diffraction (pXRD) confirmed that they retained the usual rhombic dodecahedron morphology and mean crystal size (≈300 nm), as well as crystal integrity, even after 12 h of acoustic exposure (Figures S2 and S3, Supporting Information). Results from thermogravimetric analysis (TGA) of the samples, however, reveal changes in overall weight loss percentage after different exposure times to the SRBW, as seen in **Figure 2**a. Given the well known structure of pristine ZIF-8, that is, $C_8H_{10}N_4Zn$, where each Zn atom is coordinated with 2 mIm linkers, complete framework decomposition is expected to lead to the formation of ZnO. Therefore, TGA curves of as-prepared samples were normalized so that end weights (i.e., the weight percentage of

ZnO) are equal to 100 wt%; the stoichiometric weight prior to the start of decomposition, that is, at 400 °C, is thus ≈280% (experimentally, a weight of 285% for ZIF-8, similar to that here, is common[43–45]). In particular, it can be seen that this weight diminishes with increasing acoustic exposure duration over 1, 3, and 12 h, decreasing from 280% to 279% after 1 and 3 h, respectively, and subsequently to 270% after 12 h of SRBW exposure. This would mean that in comparison to the pristine (control) ZIF-8 sample, there are ≈2 out of 20 mIm linkers missing in the unit cell after 12 h of acoustic exposure, or a defect percentage of 8.5%.

Further exposure to the SRBW beyond 12 h did not lead to appreciable increases in the level of defect creation (weight at start of decomposition ≈270%; Figure S4a, Supporting Information), although we observed a minor difference in the normalized weight at 100 °C (the temperature at which all of the trapped solvent would have been removed), which decreased from 278% at 12 h exposure to 275% at 24 h, suggesting that prolonged exposure to the SRBW could have led to the weakening of some coordination bonds, thereby resulting in the decomposition of a proportion of the mIm linkers at lower temperatures. Such destabilization of the framework at 24 h is also corroborated by the overall framework decomposition temperature, which decreased from 540 °C at 12 h to 510 °C at 24 h, as seen from the differential thermogravimetric analysis result in Figure S4b, Supporting Information, although we note that this did not lead to destruction of the framework, as confirmed by XRD analysis of the sample in Figure S4c, Supporting Information.

The existence of defects in the samples exposed to the SRBW irradiation is further corroborated by closer inspection of both X-ray photoelectron (XPS) and Raman spectroscopy of the samples. XPS, as shown in Figure 2b, indicates Zn 2p (Zn^{2+} peaks at 1021 and 1045 eV) and N 1s (peak at ≈ 300 eV) signatures consistent with those expected for pristine ZIF-8,[47–49] although the atomic compositions, calculated from the area under the individual peaks (Figure S5, Supporting Information) for N 1s and Zn 2p, show differences to that for stoichiometric ZIF-8 composition. More specifically, the N/Zn ratio is observed to decrease from 4.10 ± 0.04 in pristine ZIF-8 (control; 0 h) to 3.87 ± 0.02 at 12 h SRBW exposure, which is the equivalent to ≈1 out of 20 missing linkers in the unit cell, in rough agreement with that observed from the TGA results. This is supported by the red shift observed in the characteristic Raman peaks for the sample after 12 h of SRBW exposure at ≈175, 686, and 3115 cm^{-1} (Figure 2c–e; full spectrum shown in Figure S6, Supporting Information), corresponding to the vibrational modes associated with Zn–N stretching, imidazole ring puckering and C–H (aromatic) stretching, respectively, that indicate weakening of these bonds, which is further indication of defect creation.[50,51]

Parenthetically, we note that the defect creation under SRBW irradiation is sensitive to the various system parameters. Increasing the frequency of the device to 30 MHz (in this case, a surface acoustic wave (SAW) exists in place of the SRBW[31]), for example, or utilizing ethanol as the pressure transmitting medium in place of methanol, did not appreciably yield similar creation of defects, at least within similar timeframes (Figures S7 and S8, Supporting Information). In the case of the former, this is likely due to insufficient transmission of acoustic energy into the suspension due to the shorter acoustic penetration depth into the solution at higher frequencies. In the latter, unlike methanol, the larger size of the solvent molecules in the case of ethanol made them more difficult to penetrate the pores of the MOF[27] where they are able to transmit the acoustic radiation pressure within the structure to create appreciable permanent defects.

The N_2 adsorption isotherm (Figure S9, Supporting Information) shows an initial increase of ≈5% in the Brunauer–Emmett–Teller (BET) surface area from 1693.8 to 1781.5 m^2 g^{-1}, and the pore volume from 0.6363 to 0.6683 cm^3 g^{-1}, following 1 h of SRBW exposure compared to the pristine control. After 3 and 12 h, the surface area and pore volume decreases by roughly 1% to 2% to 1671.2 and 1657.4 m^2 g^{-1}, and, 0.6329 and 0.6223 cm^3 g^{-1}, respectively. A similar trend is observed in the argon (Ar) adsorption isotherm in **Figure 3**a, although differences in adsorption dynamics between the samples are clearly evident from the hysteresis curves. As these are only observed at relative pressures beyond $0.4 P/P_0$, this behavior is not associated with gas condensation,[52] but can rather be attributed to differences in the pore aperture configurations between the samples. In particular, the smaller hysteresis loop for the sample following 1 h of SRBW exposure (see Figure 3a inset) suggests the facilitated filling of Ar atoms within the pores of the framework and the occurrence of a reversible structural transition, as well as a reorientation of the mIm linkers at lower relative pressures of $0.15 P/P_0$ compared to the pristine control sample—possible effects of the increase in unit cell volume and pore aperture in the ZIF-8 crystals following 1 h of SRBW exposure, which allowed for the accommodation of more Ar atoms. With longer exposure durations of 3 and 12 h, we observe the hysteresis loop to increase slightly, reaching relative pressures of $0.35 P/P_0$, indicating that higher pressures are required to completely fill the pores and hence implying the increasing difficulty of Ar diffusion into the framework. While such behavior has been reported with decreasing crystal sizes,[52,53] that the opposite is true with increasing exposure durations, as seen from the SEM result in Figure S2, Supporting Information, suggests that the crystal size cannot explain the broadening of the hysteresis loop with prolonged SRBW exposure.

Taken together, the aforementioned results allude to the progression of defect formation in the material under prolonged exposure to the SRBW, with possible crystal lattice expansion at 1 h SRBW, as corroborated by the N_2 and Ar adsorption profiles, and the presence of missing-linker defects at 12 h of SRBW exposure, as inferred from the TGA, XPS, and Raman spectra. Given that linker vacancies are typically preceded by the breaking of coordination bonds, we hypothesize an intermediate state following 3 h of SRBW exposure that comprises dangling-linker defects. To validate this hypothesis, we carry out density functional theory (DFT) and Monte Carlo modeling, assuming different levels of crystal deformation following 1 h of SRBW exposure, together with the presence of dangling-linker and missing-linker defects in the crystal structure at 3 and 12 h, respectively, and show that this is in reasonable agreement with the experimental data observed.

Rietveld refinement of the pXRD data against the crystallographic structure data previously reported for a perfect ZIF-8 crystal[1] shows that the pristine control possesses the typical ZIF-8 structure with cubic space group $I\bar{4}3m$ with unit cell volume $V = 4913.8$ Å^3 (Table S1, Supporting Information). By subjecting the pXRD data of the crystals following 1 h SRBW exposure fitted against this refined crystal structure data through DFT
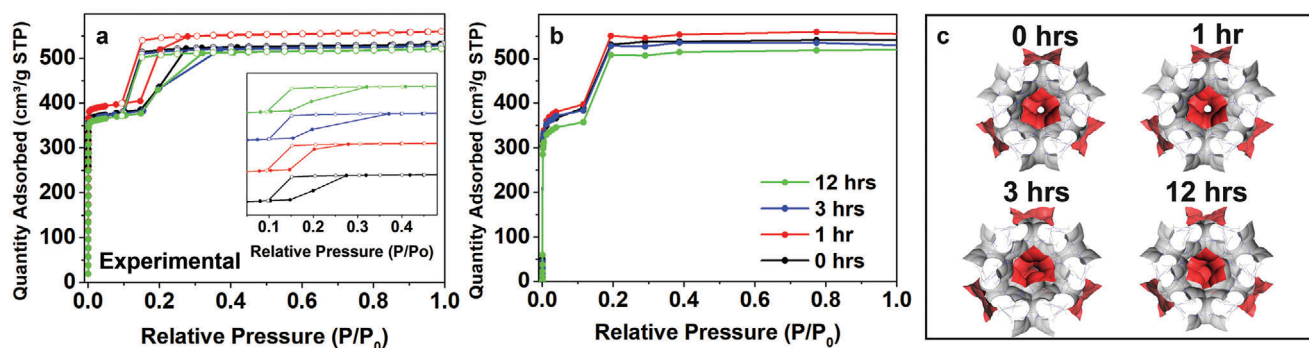
Figure 3. a) Experimental argon adsorption isotherms for the ZIF-8 samples following varying durations of SRBW exposure; the inset shows a magnification of the hysteresis region on an arbitrary vertical axis, exhibiting differences in the adsorption–desorption dynamics between the samples that allude to changes in the pore aperture; filled and hollow circles correspond to adsorption and desorption behavior, respectively. b) Predicted Ar adsorption from grand canonical Monte Carlo (GCMC) simulations using pristine (0 h) and defective (1 h: expanded framework; 3 h: dangling-linker; 12 h: missing-linker) models. c) Void analysis of density functional theory (DFT) modelled pristine and defective ZIF-8 structures showing the progressive evolution of the crystal through various local defective states with increasing SRBW exposure durations: pore expansion (1 h), dangling-linker defects (3 h), missing-linker defects (12 h).

modeling using a volume-conserving strain tensor with strain magnitudes ranging from −3% to 3% in 0.05% increments applied to the crystal lattice parameters, we determined that the best fit was obtained when a strain of 0.005 on the crystal lattice was imposed, from which an expansion of the unit cell volume to 4921.6 $Å^3$, consistent with the increased BET surface area observed for this sample, was calculated. Further refinement of the data for the 3 and 12 h SRBW exposure samples using this structure and additionally inserting guest methanol molecules into dangling-linker and missing-linker defect sites within the unit cell of the DFT model (refinement was carried out using both unexposed and defective phases, since we did not expect the defects to be present in all crystal lattices) led to distortions and broken symmetries in the unit cell with dimensions of 4924.8 and 4929.2 Å, respectively (Figure S10, Supporting Information). Despite these higher unit cell volumes, we nevertheless expect changes in the hysteresis profile, and thus decreases in Ar adsorption due to the presence of guest atoms and trapped linkers within the pores,[22,30] which is confirmed from the similarity between the experimental Ar isotherms in Figure 3a with those theoretically obtained from grand canonical Monte Carlo (GCMC) simulations in Figure 3b using the aforementioned defective (expanded framework, dangling-linker, and missing-linker) DFT models for the 1, 3, and 12 h samples, respectively. More specifically, we note the simulated Ar isotherms show an increase in Ar adsorption with the expanded framework associated with the strained structure for the 1 h exposure case, and the decrease in both surface area and pore volume by ≈2% in the 3 and 12 h SRBW exposure cases compared to the pristine control, in good agreement with that observed experimentally. This decrease in the uptake of guest Ar atoms can be attributed to the mass resistance imposed by "barriers" associated with blockage of the pore aperture by the dangling-linker and missing-linkers, as confirmed from both the simulated Ar adsorption and structural void analysis that reveal the available pore apertures for gas adsorption (Figure 3c).

As a demonstration of the potential applicability of the technique, we show the possibility of the acoustomicrofluidic platform for one-step ligand exchange under ambient conditions that takes place simultaneously with the introduction of defects into

the crystal. We deliberately choose to demonstrate the SALE with a large linker—2-aminobenzimidazole (2AbIm)—given its relative difficulty for diffusion into the framework due to steric hindrance that typically results in the exchange undesirably occurring, to a large extent, outside the framework on the crystal surface. From the ^{1}H nuclear magnetic resonance (NMR) spectra in **Figure 4**a–c for crystals obtained with the SRBW platform as well as that obtained through conventional SALE using the solvothermal technique, we find that the one-pot simultaneous defect engineering and SALE process with SRBW exposure over 12 h affords a superior ligand exchange yield of 5.15% compared to a 3.85% yield obtained with the solvothermal method (see calculations in the Experimental Section). SALE in ZIF-8 using this linker has been previously reported with nanocrystals of ≈25 nm in size[40]—an order of magnitude lower than those described here, and hence it would have been expected that the yield of exchange would have decreased with the larger crystal sizes due to lower accessible surface area.[54,55] Moreover, the SEM images and pXRD results of the samples in Figures 4d–f and 4g, respectively, show that both crystal morphology and overall structure was preserved following ligand exchange with the SRBW platform, consistent with that obtained through the solvothermal method.

In addition, the internal porosity following SRBW-facilitated ligand exchange can be observed to be maintained, as seen from the comparable BET surface area (1667.7 $m^2 g^{-1}$) to that of the original ZIF-8 prior to SALE (1676.7 $m^2 g^{-1}$), and the slight increase in the pore volume (0.6277 $cm^3 g^{-1}$ compared to 0.6130 $cm^3 g^{-1}$ for the original ZIF-8 control) due to the introduction of the larger ligand (Figure 4h). This is in contrast to the ligand exchange obtained with the conventional solvothermal method in which an approximate 10% reduction in both BET surface area and pore volume to 1497.5 $m^2 g^{-1}$ and 0.5672 $cm^3 g^{-1}$ were respectively obtained (Figure 4h). Given that the structure deformation upon ligand exchange occurs simultaneously with the introduction of the defects with the SRBW platform, we hypothesize that the invasion of methanol into the pores driven by the acoustic and hydrodynamic pressures induced by the SRBW props up the pores to prevent their collapse (which typically occurs during solvothermal ligand-exchange[56,57]), thereby leading to no loss in
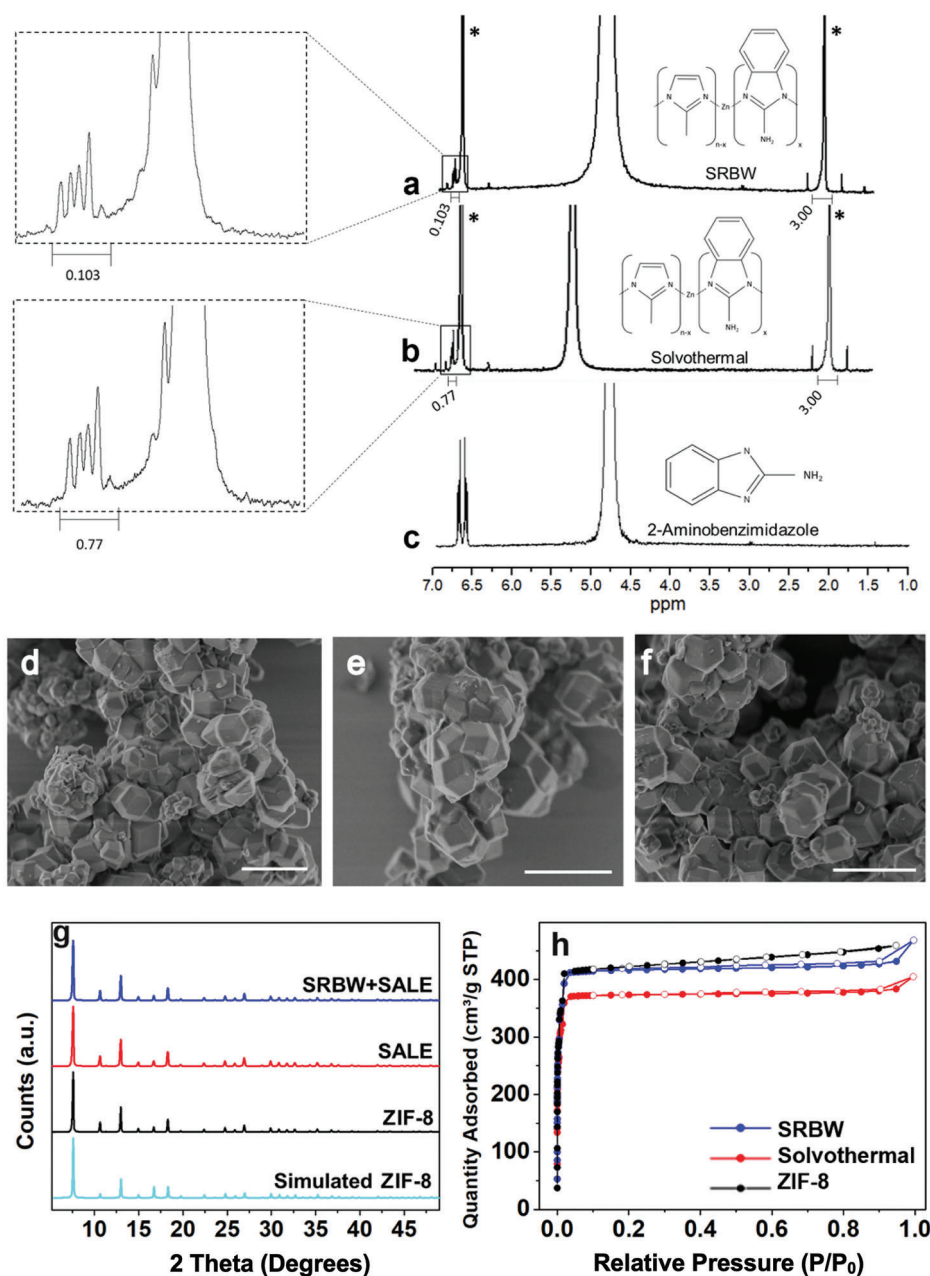
Figure 4. ^{1}H NMR spectra for a) 2-aminobenzimidazole (2AbIm) and post-SALE ZIF-8 obtained using b) the conventional solvothermal method and c) the SRBW defect engineering platform; the ligand exchange yield can be calculated from the area under the peaks in the highlighted region corresponding to ^{1}H in the benzene ring of 2AbIm. SEM images of d) the original ZIF-8 crystals prior to SALE, and the crystals obtained following SALE using e) the SRBW platform and f) the conventional solvothermal method, showing no appreciable changes in particle size or morphology; the scale bars denote 1 μm lengths. g) PXRD and h) N_2 adsorption isotherms of the original ZIF-8 control samples compared to those following SALE using the SRBW and solvothermal methods, showing preservation of the overall crystal structure and porosity following ligand exchange with the SRBW method in contrast to loss of porosity due to pore collapse with the solvothermal method.

porosity, and highlighting the potential of the SRBW platform as a promising technique for MOF ligand exchange.

3. Conclusion

In summary, we have, for the first time, explored irradiating a suspension of pre-synthesized ZIF-8 crystals in a pressure trans-

mitting medium with high frequency (MHz-order) sound waves in the form of SRBWs using a novel chipscale acoustomicrofluidic platform as a means to induce permanent structural changes in the crystal lattice at ambient temperatures, without amorphizing or carbonizing the sample. More specifically, the transmission of the SRBW energy into the medium generates a continuous recirculatory flow that imparts a MPa-order hydrodynamic

pressure together with the acoustic radiation pressure on the crystals that imposes a tensile strain on their lattice to result in irreversible lattice expansion and enhanced diffusion of guest molecules into the pore structure. Prolonging the exposure of the crystals to such irradiation then leads to the gradual introduction of, first, dangling-linker, and, subsequently, missing-linker effects, both of which further enhance host–guest interactions in the crystal. To demonstrate the practical utility of the platform, we carry out solvent-assisted ligand exchange of ZIF-8 with a relatively large linker (2-aminobenzimidazole) simultaneously with the defect engineering process on the same platform, and show the possibility for not just enhancing the ligand exchange yield compared to that obtained with the conventional solvothermal method, but also for retaining the crystal morphology and structure, as well as its porosity. These results therefore show the potential for the acoustomicrofluidic platform as a new and promising technique for MOF defect engineering for diverse applications that include enhancing gas adsorption and separation, and, catalysis, among others.

4. Experimental Section

Reagents and Chemicals: ZIF-8 (under the commercial name Basolite Z1200) and 2-aminobenzimidazole were purchased from Sigma Aldrich Pty. Ltd. (Castle-Hill, New South Wales, Australia) and used without modification. Methanol (Sigma Aldrich Pty. Ltd., Castle-Hill, New South Wales, Australia) was used as a pressure transmitting medium in which the as-synthesized ZIF-8 crystals were dispersed to a concentration of 5 mg mL^{-1}, unless otherwise specified; this was also used as the solvent for the SALE procedure.

SRBW Device: The SRBW device, similar to that previously used for MOF synthesis,[33,35] consisted of a 35 mm × 11.05 mm × 0.5 mm chip-scale single-crystal 128° *Y–X* lithium niobate (LiNbO$_3$) piezoelectric substrate on which an IDT electrode with 3.9 mm aperture widths and comprising titanium (10 nm thickness) and gold (200 nm thickness) was photolitho-graphically patterned. The width and gap of the fingers d then sets the SRBW wavelength $\lambda = 4d$, which at 348 µm corresponded to a resonant frequency of ≈10 MHz. Travelling SRBWs can then be generated along the substrate by applying a sinusoidal electric signal to the IDTs using a signal generator (N9310A, Keysight Technologies Ltd., Mulgrave, VIC, Australia) and amplifier (ZHL-5W-1+, Mini-Circuits, Brooklyn, NY, USA).

Experimental Setup: The experimental setup is shown in Figure 1 and Figure S1, Supporting Information. Briefly, 50 mg of the commercially-acquired, pre-synthesized ZIF-8 crystals were suspended in 10 mL of methanol in a long glass test tube, and bath sonicated until they were completely dispersed. The chipscale SRBW device was then mounted within the tube such that it was slightly immersed in the liquid. The lid of the tube was subsequently covered with Parafilm (Bemis Company Inc., Neenah, WI, USA) to avoid evaporation of the solution; small holes were made in the film to allow passage of the wiring to the SRBW device. Upon excitation of the IDT with an 80 V$_{rms}$ electrical signal at its resonant frequency (10 MHz), the SRBW that was generated propagated to the edge of the chip submerged in the pressure transmitting medium, into which its energy leaked to generate strong acoustic streaming (i.e., recirculation) in the liquid. The SRBW was applied continuously for 1, 3, or 12 h, following which the sample was recovered and centrifuged at 9000 rpm for 10 min. The crystals were then collected from the sample, and air dried overnight to remove the solvent within the pores prior to their characterization.

SRBW SALE: The same procedure used for the SRBW defect engineering described above was employed for the SALE procedure, but with 6× excess 2-aminobenzimidazole (175 mg) added to the methanol dispersion. The SRBW was applied continuously for 12 h, after which the sample was centrifuged at 9000 rpm for 10 min and thrice washed in methanol. The

crystals were then collected and dried in a vacuum oven overnight at 100 °C prior to characterization.

Solvothermal SALE: The solvothermal SALE method used was adapted from ref. [40]. Briefly, 200 mg of ZIF-8 was dispersed in 20 mL of methanol, and separately 702 mg of 2-aminobenzimidazole was dissolved in another 20 mL of methanol. The ZIF-8 dispersion and 2-aminobenzimidazole solution was then poured into a 50 mL Teflon lined reactor, which was sealed in a stainless-steel vessel and isothermally heated at 60 °C for 12 h, following which the crystals that were obtained were removed, cooled, and centrifuged at 9000 rpm for 10 min and thrice washed in methanol. The crystals were then collected and dried in a vacuum oven overnight at 100 °C prior to characterization.

SEM: SEM imaging (Verios 460L XHR–SEM, FEI, Hillsboro, OR, USA) was carried out with an Everhart–Thornley SE detector to characterize the morphology of the crystals prior to and following SRBW exposure and SALE; crystals were deposited on a silicon wafer and imaging was carried out at 2.0 kV.

TGA: TGA (Pyris 8000, PerkinElmer Inc., Waltham, MA, USA) was carried out to evaluate the thermal decomposition behavior of the crystals; 3–5 mg of each sample was placed in a ceramic pan and heated at a rate of 10 °C min^{-1} under air from 30 to 850 °C.

pXRD: pXRD (D8 Advance, Bruker Pty. Ltd., Preston, VIC, Australia) was conducted at room temperature and atmospheric pressure with Cu Kα radiation at 40 mA and 40 kV (λ = 1.54 Å) over a 2θ range of 5–50° with a step size of 0.02°.

XPS: XPS (K-Alpha, Thermo Fisher Scientific, Waltham, MA, USA) was conducted using a monochromated Al Kα X-ray source with a photon energy of 1486.7 eV. The spectra were collected using 50 eV pass energy, 0.1 eV step size, and 50 ms dwell time per energy step over 10 sweeps; a single sweep of the C 1s spectra was collected before and after the experiment to ensure that the X-ray beam did not damage the sample. Charge compensation was provided using a low energy Ar$^+$/e$^-$ flood gun.

Raman Spectroscopy: Samples were analyzed at room temperature using a Raman/photoluminescence spectrometer (LabRAM HR Evolution, Horiba Scientific, USA) with a laser wavelength of 532 nm, grating of 1800 g mm^{-1}, 100× objective, neutral density filter of 50 and acquisition time of 10 s for five accumulations in the range 100–3200 cm^{-1}.

Gas Adsorption and BET Analysis: N$_2$ and argon (Ar) adsorption isotherms of the control and SRBW defect engineered samples were measured at 77 K using a 3Flex Adsorption analyzer (Micromeritics, Norcross, GA, USA), whereas N$_2$ adsorption isotherms of the SALE samples were carried out at 77 K in an ASAP2460 analyzer (Micromeritics, Norcross, GA, USA). Samples were first degassed at 100 °C under vacuum for 24 h prior to all measurements.

NMR: ^{1}H NMR spectroscopy was performed in the Avance III 300 MHz Spectrometer (Bruker, Billerica, MA, USA). To quantitatively determine the percentage of exchange achieved during the SALE process, the mixed-linker products were analyzed by digestive liquid ^{1}H NMR (D$_2$O:D$_2$SO$_4$; 9:1). The NMR peaks for the 2-methylimidazolate linkers (marked by asterisks *) of the SALE ZIF-8 products represent the CH$_3$ (near 1.8 ppm) and CH=CH (near 6.5 ppm) protons, respectively. A slight positional shift was observed due to the small differences in pH of the digestive NMR solutions. For the newly introduced 2-aminobenzimidazole linkers, benzylic protons of the 2-aminobenzimidazolate linker resonate as multiplets between 6.5 and 6.7 ppm.

Ligand Exchange Yield Calculations: The ligand exchange yield was calculated from the area under the curve for ^{1}H NMR of the ZIF-8 samples following ligand exchange with 2-aminobenzimidazole (2AbIm):

$$\text{Yield} = \left(\frac{I_{\text{2AbIm}}}{I_{\text{CH}_3}} \times \frac{N_{\text{CH}_3}}{N_{\text{2AbIm}}} \right) \times 100\% \tag{1}$$

wherein I denotes the normalized area under the peaks and N denotes the number of H representative of each peak area. For the SRBW method,

$$\text{Yield} = \left(\frac{0.103}{3} \times \frac{3}{2} \right) \times 100\% = 5.15\% \tag{2}$$

2201170 (7 of 9)

**ADVANCED
SCIENCE NEWS**

www.advancedsciencenews.com

**small
methods**

www.small-methods.com

whereas, for the solvothermal method,

$$\text{Yield} = \left(\frac{0.077}{3} \times \frac{3}{2} \right) \times 100\% = 3.85\%. \qquad (3)$$

DFT Modeling: Geometry optimization of perfect, deformed, and defective models of ZIF-8 were performed using the dispersion corrected density functional theory (DFT-D3) method,[58] as implemented in the Vienna ab initio simulation package (VASP, v6.3.1; VASP Software GmbH, Vienna, Austria).[59] The initial periodic model for the ZIF-8 structure was taken from previous experimental work.[60] Electron exchange and correlation were described using the Perdew, Burke, and Ernzerhof generalized gradient approximation,[61] and projector-augmented wave potentials were used to treat core and valence electrons.[62] In all cases, a plane-wave kinetic energy cut-off of 600 eV and a Gamma-point mesh was used for sampling the Brillouin zone. To obtain different deformed models of ZIF-8, a volume-conserving strain tensor was applied to the lattice parameters with a strain magnitude that ranged from −3% to 3% in increments of 0.5%. The models were also DFT-D3 optimized, keeping the volume and the lattice parameters fixed while completely relaxing the ionic positions. Similarly, the defective models, including the dangling and missing linkers models of ZIF-8, were DFT-optimized using the same settings as described above.

Monte Carlo Simulation: The adsorption of pure Ar was simulated using the GCMC method.[63] Because the chemical potentials of adsorbate in the adsorbed and bulk phases are identical at thermodynamic equilibrium, GCMC simulation allows one to relate the chemical potentials of the adsorbate in both phases and has been widely used for simulating adsorption. Based on the atomistic model of the ZIF-8-AP (atmospheric pressure) framework,[60] the deformed model (when subjected to a tensile strain of 0.005 on the crystal lattice) that showed good agreement with the experimental XRD data (1 h SRBW exposure) was then used for the simulation. Defective models containing dangling- and missing-linkers were created based on the deformed model for further simulation representing 3 and 12 h of SRBW exposure. To describe fully the experimental behavior observed for the Ar isotherms, a combination of simulated adsorption isotherms on ZIF-8-AP and ZIF-8-HP[64] (high pressure ZIF-8 structure) before and after $0.025 P/P_0$, respectively, can predict the step shape of the experimental isotherms. A similar approach was used previously, for example to study N_2 adsorption in ZIF-8 at 77 K,[65] CO_2 adsorption in flexible MOF MIL-53,[66] and for CO_2, CH_4, and alkane adsorption in ZIF-8 at 298 K.[67] The Lennard–Jones (LJ) interactions were evaluated with a spherical cutoff equal to half of the simulation box with long-range corrections added; Coulombic interactions were calculated using the Ewald sum method. The number of trial moves in a typical GCMC simulation was 2×10^7, though additional trial moves were used at high loadings. The first 107 moves were used for equilibration and the subsequent 107 moves for ensemble averages. Five types of trial moves were attempted in the GCMC simulation, namely, displacement, rotation, and partial regrowth at a neighboring position, entire regrowth at a new position, and swapping with the reservoir. Unless otherwise mentioned, the uncertainties were smaller than the symbol sizes in the figures presented. The gas–adsorbent and gas–gas interactions were modeled as a combination of pairwise site–site LJ and Coulombic potentials. The LJ potential parameters of the framework atoms were adopted from previous work—a modified version of UFF (UFF+)[66]—and Ar was modeled using LJ parameters fitted to vapor–liquid data.[68]

Supporting Information

Supporting Information is available from the Wiley Online Library or from the author.

Acknowledgements

Conflict of Interest

The authors declare no conflict of interest.

Data Availability Statement

The data that support the findings of this study are available from the corresponding author upon reasonable request.

Keywords

[1] K. S. Park, Z. Ni, A. P. Cote, J. Y. Choi, R. Huang, F. J. Uribe-Romo, H. K. Chae, M. O'Keeffe, O. M. Yaghi, *Proc. Natl. Acad. Sci. USA* **2006**, *103*, 10186.

[2] A. Phan, C. J. Doonan, F. J. Uribe-Romo, C. B. Knobler, M. O'Keeffe, O. M. Yaghi, *Acc. Chem. Res.* **2010**, *43*, 58.

[3] U. P. Tran, K. K. Le, N. T. Phan, *ACS Catal.* **2011**, *1*, 120.

[4] M. Jia, X.-F. Zhang, Y. Feng, Y. Zhou, J. Yao, *J. Membr. Sci.* **2020**, *595*, 117579.

[5] B. Chen, Z. Yang, Y. Zhu, Y. Xia, *J. Mater. Chem. A* **2014**, *2*, 16811.

[6] Z. Fang, B. Bueken, D. E. De Vos, R. A. Fischer, *Angew. Chem., Int. Ed.* **2015**, *54*, 7234.

[7] D. S. Sholl, R. P. Lively, *J. Phys. Chem. Lett.* **2015**, *6*, 3437.

[8] S. Dissegna, K. Epp, W. R. Heinz, G. Kieslich, R. A. Fischer, *Adv. Mater.* **2018**, *30*, 1704501.

[9] A. F. Moslein, L. Dona, B. Civalleri, J.-C. Tan, *ACS Appl. Nano Mater.* **2022**, *5*, 6398.

[10] Y. Wu, Y. Li, J. Gao, Q. Zhang, *SusMat* **2021**, *1*, 66.

[11] D. Song, J. Bae, H. Ji, M.-B. Kim, Y.-S. Bae, K. S. Park, D. Moon, N. C. Jeong, *J. Am. Chem. Soc.* **2019**, *141*, 7853.

[12] J. Bae, C. Y. Lee, N. C. Jeong, *Bull. Korean Chem. Soc.* **2021**, *42*, 658.

[13] S. Yuan, L. Feng, K. Wang, J. Pang, M. Bosch, C. Lollar, Y. Sun, J. Qin, X. Yang, P. Zhang, Q. Wang, L. Zou, Y. Zhang, L. Zhang, Y. Fang, J. Li, H.-C. Zhou, *Adv. Mater.* **2018**, *30*, 1704303.

[14] A. Ferguson, L. Liu, S. J. Tapperwijn, D. Perl, F.-X. Coudert, S. Van Cleuvenbergen, T. Verbiest, M. A. Van Der Veen, S. G. Telfer, *Nat. Chem.* **2016**, *8*, 250.

[15] S. Gadipelli, W. Travis, W. Zhou, Z. Guo, *Energy Environ. Sci.* **2014**, *7*, 2232.

[16] W.-H. Lai, G.-L. Zhuang, H.-H. Tseng, M.-Y. Wey, *J. Membr. Sci.* **2019**, *572*, 410.

[17] S. Cao, T. D. Bennett, D. A. Keen, A. L. Goodwin, A. K. Cheetham, *Chem. Commun.* **2012**, *48*, 7805.

**ADVANCED
SCIENCE NEWS**

www.advancedsciencenews.com

**small
methods**

www.small-methods.com

[18] S. A. Moggach, T. D. Bennett, A. K. Cheetham, *Angew. Chem., Int. Ed.* **2009**, *48*, 7087.

[19] D. Fairen-Jimenez, S. Moggach, M. Wharmby, P. Wright, S. Parsons, T. Duren, *J. Am. Chem. Soc.* **2011**, *133*, 8900.

[20] B. Zheng, Y. Pan, Z. Lai, K.-W. Huang, *Langmuir* **2013**, *29*, 8865.

[21] Y. Sun, Y. Li, J.-C. Tan, *Phys. Chem. Chem. Phys.* **2018**, *20*, 10108.

[22] C. L. Hobday, C. H. Woodall, M. J. Lennox, M. Frost, K. Kamenev, T. Duren, C. A. Morrison, S. A. Moggach, *Nat. Commun.* **2018**, *9*, 1429.

[23] S. Chen, X. Li, E. Dong, H. Lv, X. Yang, R. Liu, B. Liu, *J. Phys. Chem. C* **2019**, *123*, 29693.

[24] J.-C. Tan, B. Civalleri, C.-C. Lin, L. Valenzano, R. Galvelis, P.-F. Chen, T. D. Bennett, C. Mellot-Draznieks, C. M. Zicovich-Wilson, A. K. Cheetham, *Phys. Rev. Lett.* **2012**, *108*, 095502.

[25] K. W. Chapman, G. J. Halder, P. J. Chupas, *J. Am. Chem. Soc.* **2009**, *131*, 17546.

[26] A. U. Ortiz, A. Boutin, A. H. Fuchs, F.-X. Coudert, *J. Phys. Chem. Lett.* **2013**, *4*, 1861.

[27] J. Im, N. Yim, J. Kim, T. Vogt, Y. Lee, *J. Am. Chem. Soc.* **2016**, *138*, 11477.

[28] J. C. Tan, T. D. Bennett, A. K. Cheetham, *Proc. Natl. Acad. Sci. USA* **2010**, *107*, 9938.

[29] F. Vermoortele, R. Ameloot, L. Alaerts, R. Matthessen, B. Carlier, E. V. R. Fernandez, J. Gascon, F. Kapteijn, D. E. De Vos, *J. Mater. Chem.* **2012**, *22*, 10313.

[30] C. Zhang, C. Han, D. S. Sholl, J. Schmidt, *J. Phys. Chem. Lett.* **2016**, *7*, 459.

[31] A. R. Rezk, J. K. Tan, L. Y. Yeo, *Adv. Mater.* **2016**, *28*, 1970.

[32] H. Ahmed, L. Lee, C. Darmanin, L. Y. Yeo, *Adv. Mater.* **2018**, *30*, 1602040.

[33] H. Ahmed, A. R. Rezk, J. J. Richardson, L. K. Macreadie, R. Babarao, E. L. Mayes, L. Lee, L. Y. Yeo, *Nat. Commun.* **2019**, *10*, 2282.

[34] H. Ahmed, X. Yang, Y. Ehrnst, N. N. Jeorje, S. Marqus, P. C. Sherrell, A. El Ghazaly, J. Rosen, A. R. Rezk, L. Y. Yeo, *Nanoscale Horiz.* **2020**, *5*, 1050.

[35] S. Marqus, H. Ahmed, A. R. Rezk, T. Huynh, A. Lawrie, D. Nguyen, Y. Ehrnst, C. Dekiwadia, L. Y. Yeo, *ACS Appl. Mater. Interfaces* **2021**, *13*, 58309.

[36] O. Karagiaridi, W. Bury, J. E. Mondloch, J. T. Hupp, O. K. Farha, *Angew. Chem., Int. Ed.* **2014**, *53*, 4530.

[37] R. J. Marshall, R. S. Forgan, *Eur. J. Inorg. Chem.* **2016**, *2016*, 4310.

[38] K. K. Tanabe, S. M. Cohen, *Chem. Soc. Rev.* **2011**, *40*, 498.

[39] T. Yamada, H. Kitagawa, *J. Am. Chem. Soc.* **2009**, *131*, 6312.

[40] C.-W. Tsai, J. Niemantsverdriet, E. H. Langner, *Microporous Mesoporous Mater.* **2018**, *262*, 98.

[41] Y. W. Abraha, C.-W. Tsai, J. H. Niemantsverdriet, E. H. Langner, *ACS Omega* **2021**, *6*, 21850.

[42] J. Friend, L. Y. Yeo, *Rev. Mod. Phys.* **2011**, *83*, 647.

[43] N. Ahmad, N. A. H. M. Nordin, J. Jaafar, N. A. N. N. Malek, A. F. Ismail, M. N. F. Yahya, S. A. M. Hanim, M. S. Abdullah, *Particuology* **2020**, *49*, 24.

[44] M. Shahsavari, P. Mohammadzadeh Jahani, I. Sheikhshoaie, S. Tajik, A. Aghaei Afshar, M. B. Askari, P. Salarizadeh, A. Di Bartolomeo, H. Beitollahi, *Materials* **2022**, *15*, 447.

[45] A. Schejn, L. Balan, V. Falk, L. Aranda, G. Medjahdi, R. Schneider, *CrystEngComm* **2014**, *16*, 4493.

[46] I. A. Lázaro, *Eur. J. Inorg. Chem.* **2020**, *2020*, 4284.

[47] F. Tian, A. M. Cerro, A. M. Mosier, H. K. Wayment-Steele, R. S. Shine, A. Park, E. R. Webster, L. E. Johnson, M. S. Johal, L. Benz, *J. Phys. Chem. C* **2014**, *118*, 14449.

[48] E. Song, K. Wei, H. Lian, J. Hua, H. Tao, T. Wu, Y. Pan, W. Xing, *J. Membr. Sci.* **2021**, *617*, 118655.

[49] S. Yang, Y. Wang, H. Li, Y. Zhan, X. Ding, M. Wang, X. Wang, L. Xiao, *J. Porous Mater.* **2021**, *28*, 29.

[50] G. Kumari, K. Jayaramulu, T. K. Maji, C. Narayana, *J. Phys. Chem. A* **2013**, *117*, 11006.

[51] B. M. Weckhuysen, Z. Ozturk, R. P. Brand, J. M. Boereboom, F. Meirer, *Chem. - Eur. J.* **2019**, *25*, 8070.

[52] S. Tanaka, K. Fujita, Y. Miyake, M. Miyamoto, Y. Hasegawa, T. Makino, S. Van der Perre, J. Cousin Saint Remi, T. Van Assche, G. V. Baron, J. F. M. Denayer, *J. Phys. Chem. C* **2015**, *119*, 28430.

[53] C. Zhang, J. A. Gee, D. S. Sholl, R. P. Lively, *J. Phys. Chem. C* **2014**, *118*, 20727.

[54] J. Wang, I. Imaz, D. Maspoch, *Small Struct.* **2022**, *3*, 2100126.

[55] K. A. S. Usman, J. W. Maina, S. Seyedin, M. T. Conato, L. M. Payawan, L. F. Dumée, J. M. Razal, *NPG Asia Mater.* **2020**, *12*, 58.

[56] Z. Hu, S. Faucher, Y. Zhuo, Y. Sun, S. Wang, D. Zhao, *Chem. - Eur. J.* **2015**, *21*, 17246.

[57] M. Taddei, R. J. Wakeham, A. Koutsianos, E. Andreoli, A. R. Barron, *Angew. Chem., Int. Ed.* **2018**, *57*, 11706.

[58] S. Grimme, S. Ehrlich, L. Goerigk, *J. Comput. Chem.* **2011**, *32*, 1456.

[59] G. Kresse, J. Hafner, *Phys. Rev. B* **1993**, *48*, 13115.

[60] K. S. Park, Z. Ni, A. P. Côté, J. Y. Choi, R. Huang, F. J. Uribe-Romo, H. K. Chae, M. O'Keeffe, O. M. Yaghi, *Proc. Natl. Acad. Sci. USA* **2006**, *103*, 10186.

[61] J. P. Perdew, K. Burke, M. Ernzerhof, *Phys. Rev. Lett.* **1996**, *77*, 3865.

[62] G. Kresse, D. Joubert, *Phys. Rev. B* **1999**, *59*, 1758.

[63] D. Frenkel, B. Smit, *Understanding Molecular Simulation: From Algorithms to Applications*, 2nd Edition, Academic Press, San Diego, CA **2002**.

[64] S. Moggach, T. Bennett, A. Cheetham, *Angew. Chem., Int. Ed.* **2009**, *48*, 7087.

[65] D. Fairen-Jimenez, S. A. Moggach, M. T. Wharmby, P. A. Wright, S. Parsons, T. Düren, *J. Am. Chem. Soc.* **2011**, *133*, 8900.

[66] N. A. Ramsahye, G. Maurin, S. Bourrelly, P. L. Llewellyn, T. Loiseau, C. Serre, G. Férey, *Chem. Commun.* **2007**, *2007*, 3261.

[67] D. Fairen-Jimenez, R. Galvelis, A. Torrisi, A. D. Gellan, M. T. Wharmby, P. A. Wright, C. Mellot-Draznieks, T. Düren, *Dalton Trans.* **2012**, *41*, 10752.

[68] M. J. McGrath, J. N. Ghogomu, N. T. Tsona, J. I. Siepmann, B. Chen, I. Napari, H. Vehkamäki, *J. Chem. Phys.* **2010**, *133*, 084106.